Weak Ferromagnetic Interaction at the Surface of the Ferrimagnetic Rb 2 Co 4 [Fe(CN) 6] 3.3 ×11H 2 O Photoexcited State

Sadaf Fatima Jafri, Marie-Anne Arrio, Amelie Bordage, Robinson Moulin, Amelie Juhin, Christophe Cartier Dit Moulin, Edwige Otero, Philippe Ohresser, Anne Bleuzen, Philippe Sainctavit

Weak ferromagnetic interaction at the surface of the ferrimagnetic $Rb_2Co_4[Fe(CN)_6]_{3.3} \cdot 11\,H_2O$ photo-excited state

Sadaf Fatima Jafri,[†] Marie-Anne Arrio,[*,†] Amélie Bordage,[‡] Robinson Moulin,[‡] Amélie Juhin,[†] Christophe Cartier dit Moulin,[¶,§] Edwige Otero,[‖] Anne Bleuzen,[*,‡] and Philippe Sainctavit[†,‖]

†*Institut de Minéralogie, de Physique des Matériaux et de Cosmochimie, UMR7590, CNRS, UPMC, IRD, MNHN, 75252 Paris Cedex 05, France*

‡*Institut de Chimie Moléculaire et des Matériaux d'Orsay, Université Paris-Sud CNRS, Université Paris-Saclay, 91405 Orsay cedex, France*

¶*CNRS, UMR 8232, Institut Parisien de Chimie Moléculaire, F-75005, Paris, France*

§*Sorbonne Université, UPMC Univ Paris 06, UMR 8232, IPCM, F-75005, Paris, France*

‖*Synchrotron SOLEIL, L'Orme des Merisiers, Saint-Aubin, France*

E-mail: marie-anne.arrio@impmc.upmc.fr; anne.bleuzen@u-psud.fr

November 14, 2017

Abstract

CoFe Prussian Blue Analogues (PBAs) are well-known for their magnetic bistability tuned by external stimuli.[1,2] The photo-switching properties are due to the electron transfer from Co^{III}_{LS}-NC-Fe^{II}_{LS} to Co^{II}_{HS}-NC-Fe^{III}_{LS} linkage, accompanied by the spin change of the Co ions (HS stands for high spin, LS for low spin). In this work, we have investigated 100 nm particles of the $Rb_2Co_4[Fe(CN)_6]_{3.3} \cdot 11\,H_2O$ PBA (named **RbCoFe**).

The photo-excited state of the PBAs was reached by red laser excitation ($\lambda = 635$ nm) and observed by X-ray absorption spectroscopy (XAS) and X-ray magnetic circular dichroism (XMCD) that are element specific probes. The XMCD measurements at the Co and Fe $L_{2,3}$ edges, probing the magnetic $3d$ orbitals, have provided a direct evidence of the antiferromagnetic interaction between the Co^{II}_{HS} and the Fe^{III}_{LS} ions belonging to the core of the particles, thus confirming the previously published, though indirect XMCD measurements at K edges.[3] Due to the surface sensitivity of XMCD at the $L_{2,3}$ edges, the magnetic properties of the particle surface have also been revealed. Surface Co^{II}_{HS}-Fe^{III}_{LS} pairs exhibit a weak ferromagnetic interaction. Thus, the magnetic structure of the photomagnetic **RbCoFe** 100 nm particles can be described as a ferrimagnetic core surrounded by a ferromagnetic shell. This finding brings new insights into the understanding of the complex magnetic properties of photo-excited **RbCoFe** and show that the surface can have different magnetic behavior than the core. This should impact the nature of magnetic coupling in nanoparticles of CoFe PBA where surface effect will dominate.

Introduction

Prussian blue Analogues (PBAs) based on Co and Fe ions, named CoFe PBAs, are well-known for their bi-stable physical properties tuned by external stimuli.[1,2] The discovery of photo-induced magnetization in the $K_{0.2}Co_{1.4}[Fe(CN)_6] \cdot 6.9\,H_2O$ PBA by Sato *et al.*[4] has opened a new field of research towards the rational design of tridimensional coordination network PBA magnets (based on Co and Fe ions,[1,4] Mn and Fe ions,[5] Fe and Cr ions,[6] Co and Os ions[7]) and derived cyanide-based molecules[1,8–11] exhibiting externally controlled reversible magnetization. Several CoFe PBAs, of chemical formula $A_xCo_y[Fe(CN)_6]_z \cdot nH_2O$, in which A is an alkali metal ion (K^+, Rb^+, Na^+, Cs^+), have been synthesized and investigated to understand thermal- and photo-induced electronic transitions.[2,12–14] Bleuzen and co-workers have participated in this effort by performing a systematic study of series of

CoFe PBAs to characterize and control the electron transfer mechanism and the associated magnetic properties.[15–25] These fascinating photomagnetic properties were found to depend upon the nature and amount of alkali cations inserted in the structure[16,17,20,26] and a series of $Rb_2Co_{4-x}Zn_x[Fe(CN)_6]_{3.3}$ PBAs with different stoichiometries has been studied to explore the photo-induced metastable state.[12,13,23] They also devoted a lot of efforts to the investigation of the $Rb_2Co_4[Fe(CN)_6]_{3.3} \cdot 11\,H_2O$ PBA (called **RbCoFe** in the following), which was chosen as a model compound for the study of the photomagnetic effect because it combines a large photomagnetic effect and a reproducible synthesis.[3,16,26–28] The ground state of **RbCoFe** is mainly composed of Co^{III}_{LS}–NC–Fe^{II}_{LS} diamagnetic pairs.[16,27] The photoswitching properties are due to the Co^{III}_{LS}–NC–Fe^{II}_{LS} to Co^{II}_{HS}–NC–Fe^{III}_{LS} photo-induced electron transfer accompanied by the spin change of the Co ions[27] (HS is high spin, LS is low spin, and by the consecutive lengthening of the Co-to-ligand bonds[27] and of the lattice parameter.[29]

Nevertheless one pertinent question about the nature of the magnetic coupling between Co^{II} and Fe^{III} ions in the photo-induced state of CoFe PBAs has remained puzzling. Further investigations of **RbCoFe** in its metastable photo-excited state by SQUID magnetometry showed magnetic ordering below a Curie temperature $T_C \approx 21$ K.[13,16,30] Nevertheless, the determination of the magnetic coupling between the Co^{II} and Fe^{III} metal ions in the photo-excited state is hampered i) by the incomplete photo-excitation of the compound in the SQUID magnetometer, which precludes any quantitative determination of the magnetization, and ii) by the thermal relaxation of the excited state, which impedes any detection of the minimum in the temperature dependence of the product of the magnetic susceptibility and temperature. In the non-photomagnetic, alkali-cation-free CoFe PBA, SQUID magnetic measurements[12–14] indicated an antiferromagnetic order below T_C. However, Pajerowski *et al.*[31] reported the parallel alignment of Co^{II} and Fe^{III} magnetic moments in a thermally quenched magnetic state of a CoFe PBA coordination polymer of chemical formula $K_\alpha Co[Fe(CN)_6]_\beta \cdot nD_2O$. The chemical selectivity of X-ray magnetic circular dichroism (XMCD), which is based on X-ray absorption spectroscopy (XAS), makes it the appropriate

tool to solve this question, since it can directly probe the magnetic moment carried by each transition metal ion.[32,33] Thus, some of us reported an XMCD study at the Fe and Co K edges of the photo-induced state of **RbCoFe** and the alkali cation free CoFe PBA.[3] XMCD at the transition metal K edges probes only the orbital magnetization of the $4p$ electrons, so that it is certainly not a direct measurement of the spin magnetic moment of the 3d electrons. By comparing the sign of the XMCD signals at the Fe and Co K edges in the ferrimagnetic alkali cation free CoFe PBA and in the photo-induced state of **RbCoFe**,[3] it was proposed that the two magnetic structures are likely to be similar. However, the antiparallel alignment of the Co^{II} and Fe^{III} magnetic moments had never been directly probed.

Here, we report on the thermally-induced and photo-induced charge transfert in **RbCoFe** detected by XAS, coupled to the XMCD results of the $Co^{II}_{HS}Fe^{III}_{LS}$ photo-induced state. Both XAS and XMCD signals have been recorded at Fe and Co $L_{2,3}$ edges. In a first section, we present the experimental and theoretical tools that were needed for the present study. The second section is dedicated to the presentation of the experimental results for which simulation calculations have been developed. The last section is a discussion of the obtained results with an emphasis on the Co(II)-Fe(III) magnetic interaction in the metastable, photo-excited state.

Experimental and theoretical details

Synthesis and characterization

RbCoFe was synthesized using the procedure reported by Bleuzen *et al.* [16] The sample was characterized by elemental analysis, X-ray diffraction and Transmission Electron Microscopy. The particles are regular and homogeneous cubes of 100nm-side (**S.I. section I**). Polycrystalline $K_3[Fe(CN)_6]$ and $K_4[Fe(CN)_6]$ reference compounds were bought from Merck company.

The photo-magnetic property was checked by SQUID magnetometry measurements on

microcrystalline powder.[34] The sample was irradiated at 10 K with a red laser diode ($\lambda = 635$ nm) and the field dependence of the magnetization of the **RbCoFe** photo-excited state was investigated at 2 K, 5 K and 20 K. The magnetic measurements are reported in Supporting Information **(S.I. section I)**.

XAS and XMCD measurements.

XAS and XMCD signals were measured at the Fe and Co $L_{2,3}$ edges on the DEIMOS beamline at SOLEIL synchrotron (France).[35] Two undulators, namely an Apple-II helical undulator and an EMPHU undulator with different functions, work as the photon sources. The Apple-II helical undulator delivers a flux of circularly and linearly polarized X-rays in the energy range 350–2500 eV. It was used for XAS and XMCD measurements. The EMPHU undulator is built with electromagnets and permanent magnets tailored to deliver circularly polarized X-rays with a fast switching of the X-ray polarization state (between 1 Hz and 5 Hz). It was used to record the XMCD detected magnetization curves. The main end station at DEIMOS beamline consists of the cryogenic magnet CroMag, which can provide a $\pm$ 7 T magnetic induction along the incoming X-ray beam. The sample is attached to a variable temperature insert that controls the sample temperature between 1.5 K and 370 K.

To compensate for possible errors induced by spurious signals, the XMCD signal was measured by taking the difference of four XAS spectra recorded for left and right polarized X-rays with the external magnetic induction $\boldsymbol{B}$ parallel or antiparallel to the direction of the X-ray propagation vector. By definition, the XMCD signal is given by $\sigma_{\mathrm{XMCD}} = \sigma^- - \sigma^+$, where $\sigma^- = [\sigma_L(\boldsymbol{B}^-) + \sigma_R(\boldsymbol{B}^+)]/2$ and $\sigma^+ = [\sigma_L(\boldsymbol{B}^+) + \sigma_R(\boldsymbol{B}^-)]/2$. σ_L (σ_R) is the cross-section with left (right) polarized X-rays, and $\boldsymbol{B}^+$ ($\boldsymbol{B}^-$) the magnetic induction parallel (antiparallel) to the X-ray propagation vector. With these definitions, a negative XMCD signal at the L_3 edge of $3d$ metals corresponds to a magnetic moment pointing in the same direction as the external magnetic induction. In the following, XAS refers to $\sigma_{\mathrm{XAS}} = (\sigma^- + \sigma^+)/2$ and XMCD to $\sigma_{\mathrm{XMCD}} = \sigma^- - \sigma^+$. The background is subtracted from the XAS spectra

using two arctangent functions that model the $2p_{3/2} \rightarrow$ continuum and $2p_{1/2} \rightarrow$ continuum transitions.[36] The XAS spectra are then normalized to 1 at the maximum of the L_3 edge and the XMCD signals are normalized in proportion.

RbCoFe was dropcast ed in milli-Q water on a silicon wafer, which was mounted on a copper sample holder. $K_3[Fe(CN)_6]$ and $K_4[Fe(CN)_6]$ polycrystals were grinded and stick to a conductive carbon tape. All spectra are recorded under UHV conditions in the total electron yield mode, which results in spectral information arising from the sample surface ($\sim$ 60% of the signal comes from the top 2 nm). During the measurements, we carefully checked that **RbCoFe** remains (i) free from radiation damage from the X-ray beam, (ii) with no degradation related to the UHV environment and (iii) stable in temperature, as it undergoes several heating and cooling cycles.

Three kinds of measurements were performed. **First**, we investigated the photo-induced electron transfer. Fe and Co $L_{2,3}$ edges were recorded at 200 K where the compound is mainly composed of $Co^{III}_{LS}Fe^{II}_{LS}$ diamagnetic pairs.[26] Then, the sample was cooled down to 2 K, where it has been irradiated with a red laser ($\lambda = 635$nm, P= 20mW) for 5 hours in order to induce the electron transfer towards the photo-excited state which contains a significant amount of $Co^{II}_{HS}Fe^{III}_{LS}$ pairs. The laser was switched off to acquire XAS and XMCD data in the photo-excited state. At 2 K the lifetime of the **RbCoFe** photo-excited state is larger than a week.[22] **Second**, XMCD-detected magnetization curves were measured as a function of the applied magnetic induction to determine the nature of the magnetic coupling between the Fe^{III} and Co^{II} ions. For such measurements, the monochromator is set at the energy of the maximum intensity (in absolute value) of the XMCD signals. The XMCD intensity is measured by sweeping the intensity of the external magnetic induction, step by step, between +6.5 T and -6.5 T and by flipping the circular polarization at each step of induction. Such XMCD detected magnetization curves were recorded for temperatures ranging between 2 K and 30 K. **Third**, Fe and Co $L_{2,3}$-edges XMCD signals were recorded in the photo-excited state at lower magnetic induction values (0.45 T and 1.5 T). The reversibility of the photo-

induced electron transfer process was also checked by measuring X-ray absorption spectra after complete thermal cycles between 300 K and 4 K.

Ligand Field Multiplet calculations

LFM Theory describes atomic-like ground and excited states, such as those involved in the $L_{2,3}$ edges of $3d$ transition elements in iono-covalent compounds. LFM theory and its practical implementation for the calculation of XAS spectra are due to the pioneering work by Theo Thole,[37] based on the atomic theory developed by Cowan[38] and the ligand field interactions (*i.e.*, symmetry) described by Butler.[39] The calculated XAS within the LFM theory have already been published for the **RbCoFe** compound by our groups.[27] In the present work, we used the calculated Co^{II}_{HS} and Co^{III}_{LS} XAS to determine the $Co^{II}_{HS}/Co^{III}_{LS}$ ratios. For Fe^{II}_{LS} and Fe^{III}_{LS}, we used experimental references. Octahedral environments were considered for Fe and Co ions (see **S.I. section IV**). The $|i\rangle$ initial eigenstates were calculated for the ground state and all the states populated at finite temperatures in order to determine the expectation values $\langle i|L_z|i\rangle$ and $\langle i|S_z|i\rangle$ and then to compute the magnetization curves. For the Fe^{III}_{LS} ion bonded to a cyanido ligand, a metal to ligand charge transfer model (MLCT) is employed to account for π back bonding as described previously.[40,41] The initial state of the $3d^5$ Fe^{III} ion was taken as a linear combination of the two configurations $|2p^6 3d^5\rangle$ and $|2p^6 3d^4 L^-\rangle$, where L^- stands for one additional electron on a ligand orbital.

Results and detailed analysis

Evidence of the Light-induced metal-to-metal electron transfer

Co and Fe $L_{2,3}$-edges spectra were recorded at 200 K and at 2 K after 5 hours of laser irradiation in order to characterize the $Co^{III}_{LS}Fe^{II}_{LS} \rightarrow Co^{II}_{HS}Fe^{III}_{LS}$ electron transfer. The reversibility of the electron transfer was carefully checked by recording the spectra at both edges along several temperature cycles such as 200 K $\rightarrow$ 4 K $\rightarrow$ laser irradiation $\rightarrow$ 200 K (**S.I. section**

III). We monitored the laser-irradiation by measuring Co and Fe $L_{2,3}$-edges spectra at different time of irradiation (S.I. section II). After 5 hours, we could detect no more changes and thus concluded that the electron transfer was complete. It is to be noted that "complete electron transfer" here means that the photo-excited state of the compound is reached and it does not imply that all the $Co^{III}_{LS}Fe^{II}_{LS}$ pairs of the ground state were photo-excited into $Co^{II}_{HS}Fe^{III}_{LS}$ pairs.

The normalized spectra are shown in Figure 1 and compared with LFM calculated XAS for Co^{II}/Co^{III} ion and experimental reference XAS for Fe^{II}/Fe^{III} ions ($K_4[Fe(CN)_6]$ and $K_3[Fe(CN)_6]$). The XAS at 200 K and 2 K after laser excitation are similar to the one previously obtained by our groups.[27] At the Co L_3 edge, peaks *a'* (775.6 eV), *b'* (776.8 eV), *c'* (777.3 eV) and *d'* (778.1 eV) are attributed to the Co^{II}_{HS} XAS, whereas peak *e'* (779.8 eV) comes from the Co^{III}_{LS} XAS, as can be seen by comparison to the LFM calculation in Figure 1. Co^{III}_{LS} and Co^{II}_{HS} are both present in the 200 K ground state and the 2 K photo-excited state, but at 200 K, peak *e'* (779.8 eV) is 1.6 times more intense than *b'*, *c'* and *d'*, which indicates that the **RbCoFe** ground state contains Co^{III}_{LS} and Co^{II}_{HS} ions. After laser excitation at 2 K, peak *e'* looses ∼70% of its intensity while the intensity of *b'*, *c'* and *d'* increases, which indicate that most of the Co^{III}_{LS} ions were transformed into Co^{II}_{HS} ions in the **RbCoFe** photo-excited state. At the Fe L_3 edge, from the comparison with reference experimental spectra (see Figure 1), it is obvious that peak *a* (705.8 eV) is characteristic of Fe^{III}_{LS} ion. The other main peaks (*b* at 709.5 eV, *c* at 711.1 eV and *d* at 712.2 eV) come from the $Fe^{III}_{LS}/Fe^{II}_{LS}$ mixture. The 200 K ground state and the 2 K photo-excited state both contain such a mixture. At 200 K, the low intensity of peak *a* (∼35% of peak *b*), when compared to reference XAS spectra, indicates that the **RbCoFe** ground state is mainly composed of Fe^{II}_{LS} ions. After laser excitation at 2 K, the intensity of peak *a* increases (to almost 90% of peak *b*) which indicates that most of the Fe^{II}_{LS} ions are transformed into Fe^{III}_{LS} ions in the **RbCoFe** photo-excited state. The changes observed at both edges are fully consistent with our previous measurements at $L_{2,3}$ edges on **RbCoFe**[26–28,42] and they are the genuine

signature of the photo-induced $Co^{III}_{LS}Fe^{II}_{LS} \rightarrow Co^{II}_{HS}Fe^{III}_{LS}$ electron transfer.

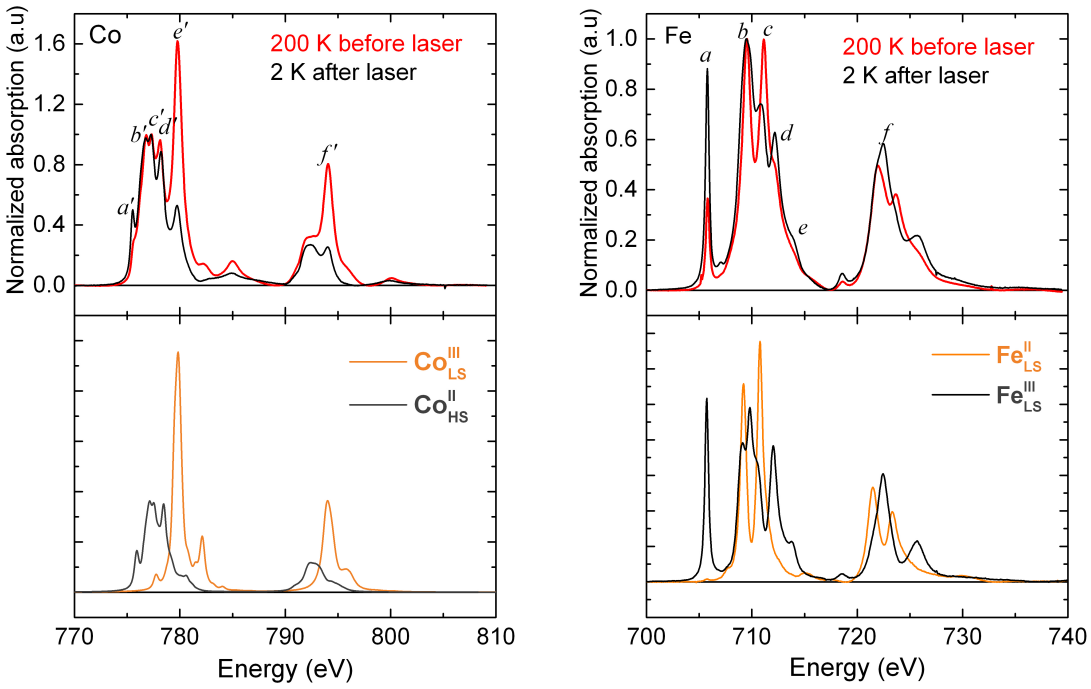

Figure 1: (Top) Experimental XAS spectra at the Co (left) and Fe (right) $L_{2,3}$ edges before laser irradiation at 200 K (red line) and at 2 K after 5 hours laser irradiation (black line). (Bottom) Left: Calculated XAS spectra at the Co $L_{2,3}$ edges for octahedral Co^{III}_{LS} (orange line) and Co^{II}_{HS} (gray line) ions. Right: Experimental XAS spectra at the Fe $L_{2,3}$ edges for reference compounds: $K_4[Fe(CN)_6]$ for Fe^{II}_{LS} (orange line) ion and $K_3[Fe(CN)_6]$ for Fe^{III}_{LS} (gray line) ion.

A quantification of the Co^{III}_{LS} and Co^{II}_{HS} (resp. Fe^{III}_{LS}, Fe^{II}_{LS}) species in both states was performed from linear combinations of the calculated reference spectra (resp. reference experimental spectra) (S.I. section IV). The errors on the percentages obtained from the fitting procedures are close to ±5 %. For the **RbCoFe** ground state, the linear combinations lead to 40 % of Fe^{III}_{LS} and 60 % of Fe^{II}_{LS} and, 60 % of Co^{II}_{HS} and 40 % of Co^{III}_{LS}. For the **RbCoFe** photo-excited state, the fit leads to 75 % of Fe^{III}_{LS} and 25 % of Fe^{II}_{LS}, and 84 % of Co^{II}_{HS} and 16 % of Co^{III}_{LS}. These percentages for Fe and Co species in the ground and in the photo-excited states are very close to those that were already determined by XAS at the $L_{2,3}$ edges for the same compound,[26–28] but they are significantly different from those determined

by spectroscopies performed in transmission mode at K-edges,[34] by X-ray diffraction[29] or by magnetometry,[17] which probe the whole volume of the sample. The XAS spectra at the Co and Fe K edges of **RbCoFe** at 300 K and at 10 K after irradiation are given in supporting information (**S.I. section V**) as an example. Such discrepancies between the results obtained by XAS at the $L_{2,3}$ edges and by measurements probing the whole sample volume were already mentioned in previous studies.[26–28,42] They were ascribed to the limited probing depth due to the electron yield detection mode used for $L_{2,3}$ edges and the associated important contribution of surface species. The large amount of Co^{II}_{HS} and Fe^{III}_{LS} species in the ground state of **RbCoFe** detected by XAS at the $L_{2,3}$ edges can be linked to the large amount of Co^{II}_{HS} species detected by XAS at the Co K edge in the ground state of 5 nm nanoparticles of **RbCoFe** with exactly the same chemical composition[34,43] and to the high magnetization value before irradiation in photomagnetic nanoparticles with a comparable Co/Fe ratio.[44] In all these studies the contribution of surface species is enhanced due either to the detection mode or to a larger surface area to volume ratio, which allow us to conclude that the Co^{II}_{HS} and Fe^{III}_{LS} supplementary species in the ground state of **RbCoFe** are surface species. In the following, we see how the surface affects the magnetic properties.

Magnetic properties of the RbCoFe photo-excited state

In this section, we only describe the results concerning the photo-excited state of **RbCoFe**, obtained at 2 K after laser excitation.

XMCD measurements at 6.5 T

We recorded the XMCD signals at the Fe and Co $L_{2,3}$ edges in a 6.5 T external magnetic induction in order to get magnetic information on the photo-excited state of **RbCoFe**. At 6.5 T, the magnetization is expected to be close to saturation. The XAS and XMCD signals are displayed in Figure 2.

The Co $L_{2,3}$ edges XMCD signal is characterized by an intense negative peak (γ', at 777.3 eV), that reaches 95% of the intensity of the *c'* peak of the X-ray absorption spectrum. The shape and intensity are characteristic of an octahedral Co^{II}_{HS} ion[45] in PBA. The negative sign of XMCD indicates that the Co^{II}_{HS} magnetic moments are oriented parallel to the external magnetic induction. Taking into account the 84% Co^{II}_{HS} contribution to XAS (from previous section), the XMCD intensity at peak γ' is indeed $\simeq$113% (=0.95/0.84) of XAS peak *c'*. Therefore, the XMCD intensity indicates that Co^{II}_{HS} ion is close to its magnetic saturation, as expected from LFM calculation on similar systems.[46]

At the Fe $L_{2,3}$ edges, three peaks of similar intensity are observed (peak α at 705.7 eV, peak β at 709.3 eV and peak γ at 709.9eV). Surprisingly, the shape is quite different from the one observed for $K_3[Fe(CN)_6]$ (**S.I. Figure S9**), although the Fe^{III}_{LS} local environment is expected to be similar to the one in $K_3[Fe(CN)_6]$, *i.e* six cyanido ligands. Peak β is not present in the $K_3[Fe(CN)_6]$ XMCD signal and the XMCD intensity is quite small. The XAS peak *a* is due to Fe^{III}_{LS} species and does not contain any contribution from Fe^{II}_{LS} ions. In the case of photo-excited **RbCoFe**, the XMCD intensity at peak α (coming only from Fe^{III}_{LS}) is $\approx$17 % of XAS peak *a* whereas, for $K_3[Fe(CN)_6]$, it reaches 80 %. As the peaks *a* and α come from Fe^{III}_{LS} species only, the small XMCD intensity can not be attributed to the presence of diamagnetic Fe^{II}_{LS} ions in **RbCoFe**. In addition, the XMCD negative sign at peak α indicates that the average Fe^{III}_{LS} magnetic moment is parallel to the external induction and therefore parallel to the Co^{II}_{HS} magnetic moment. The small intensity of the photo-excited **RbCoFe** XMCD signal can be due to: (i) magnetic disorder in the Fe^{III} sub-lattice that could be caused by surface effect, but it is not supported by the fact that Co^{II} magnetic moments are fully oriented; (ii) only a small part of the Fe^{III}_{LS} ions would be in antiferromagnetic interaction with the Co^{II}_{HS} ions, whereas the majority of Fe^{III}_{LS} ions would have their magnetic moments parallel to the Co^{II}_{HS} ones. The latter Fe^{III}_{LS} ions might thus be paramagnetic or in ferromagnetic interaction with the Co^{II}_{HS} ions. This hypothesis is possible if the population of the two Fe^{III}_{LS} species (with parallel and antiparallel magnetic moments) are close.

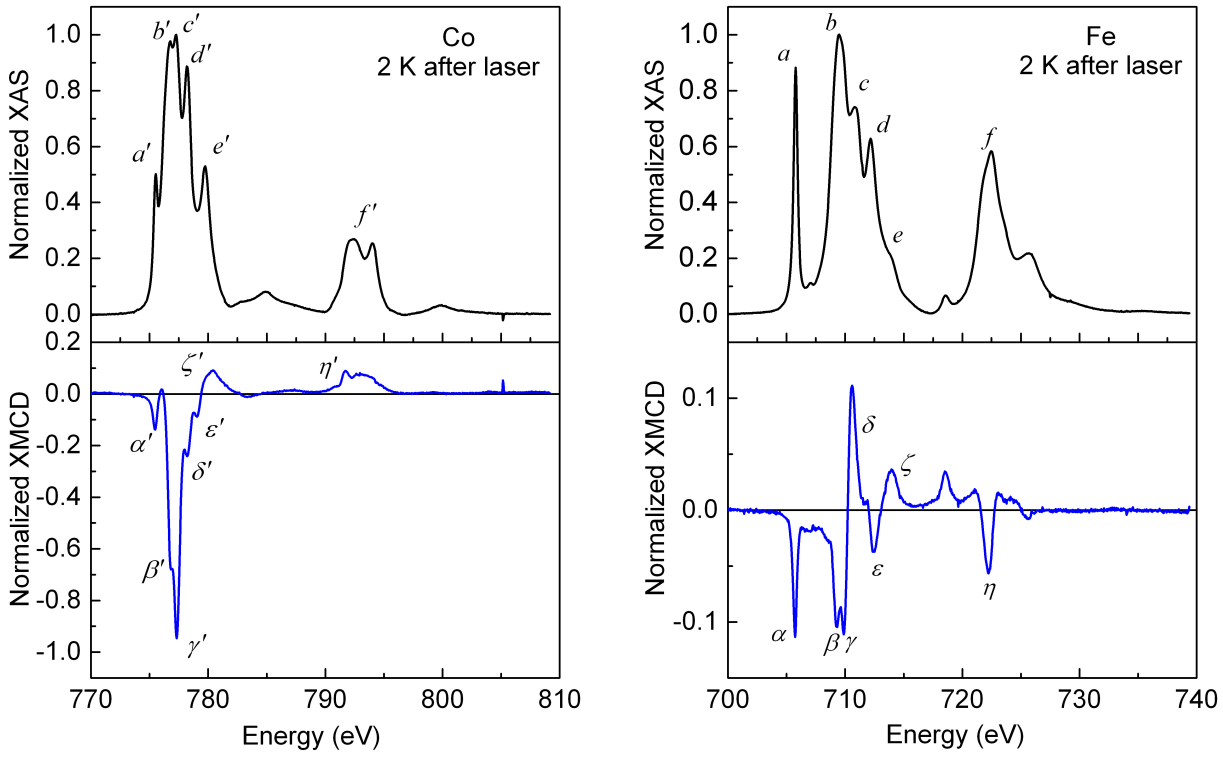

Figure 2: Experimental XAS (black line) and XMCD (red line) spectra at Co (left) and Fe (right) $L_{2,3}$ edges at 2 K after a 5 hours laser irradiation.

Element specific magnetization curves

The element specific magnetization curves, corresponding to the magnetic-field dependence of the opposite of the intensity of the XMCD signal measured at a fixed energy at 2 K, are reported for Co^{II} and Fe^{III} in Figure 3. The fixed energy is given by the maximum absolute intensity of the XMCD signal for the Co ions and by the maximum of peak alpha for the Fe ions.

At the Co L_3 edge, the monochomator was set to the energy of peak γ' (777.3 eV). One observes a sharp rise of the magnetization in the first 500 mT followed by a linear increase of magnetization. This monotonous variation indicates that the Co^{II} ions are always magnetized parallel to the external magnetic induction. Nevertheless the Co^{II} magnetization seems

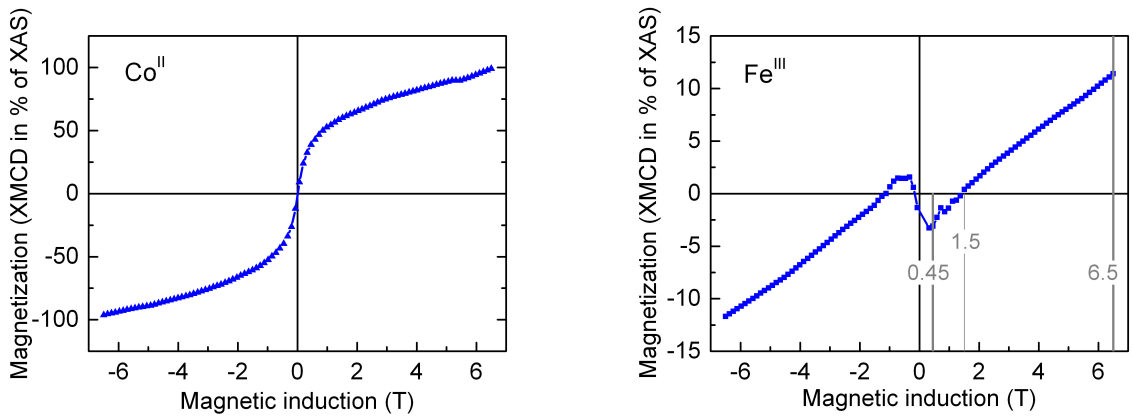

Figure 3: XMCD detected magnetization curve for Co^{II} ion (left) and Fe^{III} ion (right) at 2 K recorded at E = 777.3 eV and E = 705.7 eV respectively.

difficult to saturate in inductions as large as 6.5 T. At the Fe L_3 edge, the magnetization curve was measured at the energy of the maximum of peak α (705.7 eV), that is present for **RbCoFe** as well as for $K_3[Fe(CN)_6]$. Between 1.5 T and 6.5 T, one observes a linear variation of the magnetization parallel to the external magnetic induction and between -1.5 T and $+1.5$ T, there is a clear inversion of the magnetization showing that the Fe^{III} magnetization is antiparallel to the external magnetic induction. Firstly, the direct observation of the element specific magnetization curves shows, without ambiguity, that between -1.5 T and $+1.5$ T, the average magnetization for the Co and Fe sub-lattices corresponds to antiferromagnetically coupled Fe^{III} and Co^{II} ions. The Co^{II} magnetic moment being larger than the Fe^{III} one, it is parallel to the external magnetic induction. Secondly, the sign change of the resulting magnetization of the Fe sub-lattice with increasing magnetic induction cannot be due to a reversal of all magnetic moments carried by the Fe^{III}_{LS} ions when the Zeeman effect becomes stronger than exchange interaction. Indeed such an effect would give a distinctive signature on SQUID measurements that has never been observed. Another explanation would stem from the presence of two sites of Fe^{III}_{LS} ions with parallel and antiparallel magnetizations to the external magnetic induction, the resulting magnetization being dominated by one or the other site depending on the strength of the external magnetic induction. Only this hypothesis is coherent with the complex shape and the small intensity of the XMCD signal

(see above).

From the literature and as checked by our SQUID magnetic measurements, the Curie temperature of **RbCoFe** is 21 K so that we expect that the signature of the ferrimagnetism will disappear if the temperature is raised from 2 K up to 30 K. We have recorded Fe^{III} and Co^{II} XMCD detected magnetization curves at T = 2 K, 4 K, 10 K, 20 K and 30 K (reported in S.I. **section VII**). As we approach the Curie temperature, the signature of the antiferromagnetic phase (*i.e.* the non-monotonous behavior of the Fe^{III} magnetization curve) tends to disappear. At 30 K the magnetization curve is almost a straight line with no accident in the region between ±1.5 T. In Fig. 4, we have reported the slope of the magnetization curves at $\boldsymbol{B} = 0$ T as a function of the temperature. For Co^{II}, the slope of the magnetization curves remain positive for all temperature values and decreases when temperature is increased. The slope of the Fe^{III} magnetization is negative and it decreases in absolute values when the temperature increases from 2 K to 30 K. Around 20 K, the slope changes sign and becomes positive. This means that the contribution from the antiferromagnetic part is no more dominating over the contribution from the paramagnetic or ferromagnetic part.

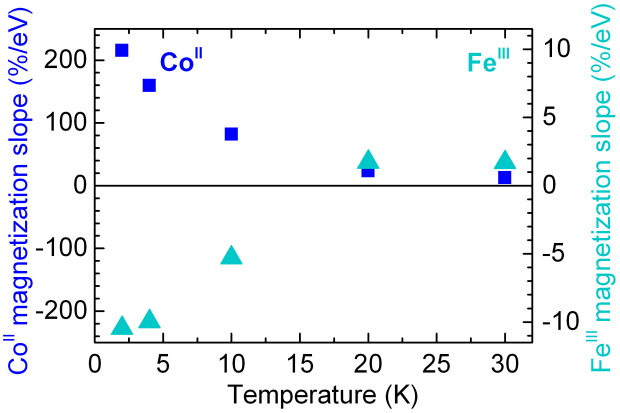

Figure 4: Slope at $\boldsymbol{B} = 0$ T for the Fe^{III} (▲) and Co^{II} (■) magnetization curves as a function of temperature obtained from XMCD detected magnetization curves (shown in S.I. section VII, Figure S9).

This series of measurements proves that the antiferromagnetic part is indeed the ordered phase measured by SQUID and which corresponds to the magnetic behavior of the whole

sample volume. From the present XMCD investigation, which mainly probes the surface of the sample, we can propose that **RbCoFe** in its photo-excited state is built from an antiferromagnetic part corresponding to the core of the particles, and an extra part corresponding to the surface, where the Fe^{III}_{LS} and Co^{II}_{HS} magnetic moments are parallel. Whether the two ions are non-coupled paramagnetic ions or are in ferromagnetic interaction cannot be clarified at this point.

In the following, for reader facility, we will refer to ${}^{AF}Fe^{III}_{LS}$ for the Fe^{III}_{LS} ions in antiferromagnetic interaction with Co^{II}_{HS}, and to ${}^{P/F}Fe^{III}_{LS}$ for the paramagnetic Fe^{III}_{LS} ions either or not in ferromagnetic interaction with Co^{II}_{HS}. The presence of two Fe^{III}_{LS} sites with opposite directions of the magnetic moments explain the small Fe^{III}_{LS} XMCD intensity at 6.5 T in the **RbCoFe** photo-excited state compared to $K_3[Fe(CN)_6]$. Indeed the XMCD signal would result from the combination of a mainly positive contribution coming from ${}^{AF}Fe^{III}_{LS}$ and a mainly negative contribution coming from ${}^{P/F}Fe^{III}_{LS}$.

Analysis of the Co^{II}_{HS} and Fe^{III}_{LS} XMCD signals

The Fe^{III} magnetization curve at 2 K (Figure 3) obviously reveals two regimes associated with the different signs of the XMCD signal, where the antiferromagnetic phase is either dominating or dominated by the paramagnetic/ferromagnetic phase depending on the strength of the external magnetic induction. To get more information, we have recorded the XMCD signals for the three following external magnetic inductions:

(i) $\boldsymbol{B}_1 = 6.5$ T, where the Fe^{III} average magnetization is parallel to the external magnetic induction (presented in the previous subsection),

(ii) $\boldsymbol{B}_2 = 1.5$ T, where the Fe^{III} average magnetization is almost zero, and

(iii) $\boldsymbol{B}_3 = 0.45$ T, where the Fe^{III} average magnetization is antiparallel to the external magnetic induction.

At the Co $L_{2,3}$ edges, since the Co^{II} magnetic moment is always parallel to the external magnetic induction, there is no easy way to separate the contributions from the Co^{II} ions

belonging to the antiferromagnetic core or to the paramagnetic/ferromagnetic surface. We have recorded the Co $L_{2,3}$ XMCD signal at $\boldsymbol{B}_1 = 6.5$ T and only $\boldsymbol{B}_3 = 0.45$ T.

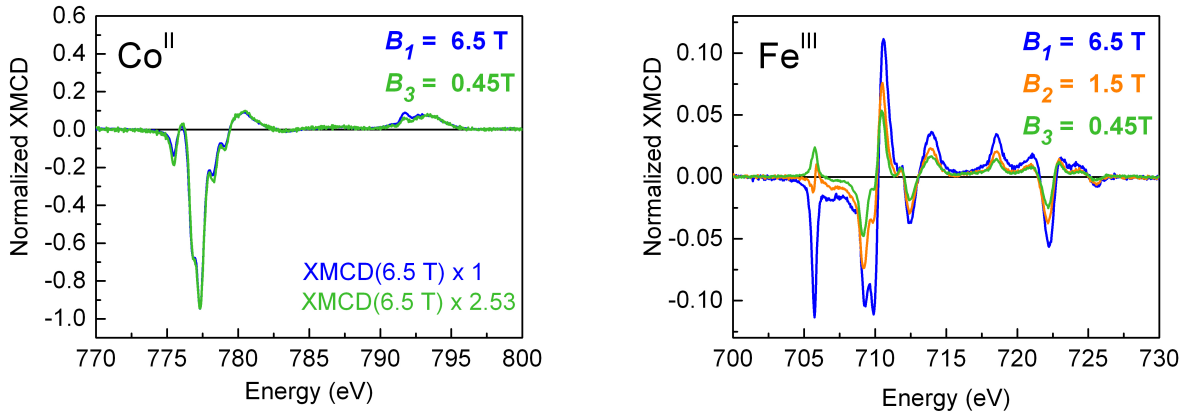

Figure 5: (Left) XMCD signals at Co $L_{2,3}$ edges measured at T = 2 K at $\boldsymbol{B}_3 = 0.45$ T and $\boldsymbol{B}_1 = 6.5$ T. The signal at 0.45 T is scaled by 2.53 so that γ' peak superimposes with γ' peak at 6.5 T. (Right) XMCD signals at Fe $L_{2,3}$ edges recorded at T = 2 K and $\boldsymbol{B}_1$= 6.5 T (blue line), $\boldsymbol{B}_2$= 1.5 T (orange line), $\boldsymbol{B}_3$= 0.45 T (green line).

The various XMCD signals at the Fe and Co $L_{2,3}$ edges are reported in Figure 5. Both Co^{II} XMCD signals for $\boldsymbol{B}_1$ and $\boldsymbol{B}_3$ have almost the same shape. The Co^{II} XMCD signal at $\boldsymbol{B}_1$ is equal to 2.5 times the one at $\boldsymbol{B}_3$, as observed in the Co^{II} magnetization curve in Figure 3. This indicates that the Co^{II} ions are in very similar environments, whether they are present in the antiferromagnetic or in the paramagnetic/ferromagnetic phase, and that the Co^{II} magnetization is always parallel to the external magnetic induction for both phases. On the contrary, one observes that the shape of the Fe^{III} XMCD signals varies quite a lot with the intensity of the induction. For $\boldsymbol{B}_2 = 1.5$ T, the intensity of the XMCD signal is small but not zero over the whole energy range: at 705.7 eV (maximum of peak α at 6.5 T), where the magnetization curve was recorded, the intensity of the XMCD signal is close to zero with a derivative shape of the signal but the intensity of the other peaks is substantial. The derivative shape of peak α indicates that the Fe^{III} ions are present in at least two different sites with slightly different environments Peak γ is strongly reduced and remains negative, even at $\boldsymbol{B}_3 = 0.45$ T. Its intensity decreases much with the induction, since the β/γ ratio

are approximately 1:2:4 for $\boldsymbol{B}_1$:$\boldsymbol{B}_2$:$\boldsymbol{B}_3$ respectively. This further confirms that peak γ is a signature of the ${}^{AF}\mathrm{Fe}^{\mathrm{III}}_{\mathrm{LS}}$ ions. Peaks β and δ are reduced respectively by 0.7 and 0.3 and remain with the same signs for all inductions; they are the signature of the ${}^{P/F}\mathrm{Fe}^{\mathrm{III}}_{\mathrm{LS}}$. Peak α is the only feature whose sign is reversed at $\boldsymbol{B}_3 = 0.45$ T, and is therefore the strongest evidence for the existence of an antiferromagnetic coupling between some of the $\mathrm{Fe}^{\mathrm{III}}_{\mathrm{LS}}$ ions and some of the $\mathrm{Co}^{\mathrm{II}}_{\mathrm{LS}}$ ions.

We used these three XMCD measurements to separate the different $\mathrm{Fe}^{\mathrm{III}}$ ion sites. Information can be gained on the antiferromagnetic phase from linear combinations of $\mathrm{Fe}^{\mathrm{III}}$ XMCD signals at 6.5 T and 0.45 T. The β peak comes from the ${}^{P/F}\mathrm{Fe}^{\mathrm{III}}_{\mathrm{LS}}$ ions, so that if the XMCD signals at 0.45 T is scaled for the β features to superimpose, the difference between the two rescaled XMCD signals gives an XMCD signal for the ${}^{AF}\mathrm{Fe}^{\mathrm{III}}_{\mathrm{LS}}$ ions, noted $\left[\sigma^{AF}_{XMCD}\right]^{raw}$. Figure 6 (upper panel) shows the rescaled XMCD signals and the $\left[\sigma^{AF}_{XMCD}\right]^{raw}$ difference. The $\left[\sigma^{AF}_{XMCD}\right]^{raw}$ signal is similar to the XMCD signal for $K_3[Fe(CN)_6]$ but for an opposite sign (see Figure 6, lower panel). Indeed, this is consistent with the fact that the ${}^{AF}\mathrm{Fe}^{\mathrm{III}}_{\mathrm{LS}}$ local environment is expected to be similar to the one in $K_3[Fe(CN)_6]$. One then obtains the paramagnetic/ferromagnetic $\left[\sigma^{P/F}_{XMCD}\right]^{raw}$ contribution by subtracting to the XMCD signal at 6.5 T the antiferromagnetic signal, scaled by a multiplication factor to account for the amplitude variation with induction. The obtained $\left[\sigma^{P/F}_{XMCD}\right]^{raw}$ XMCD signal is similar to the XMCD signal for $K_3[Fe(CN)_6]$ with the same sign. Detailed extraction of the ${}^{AF}\mathrm{Fe}^{\mathrm{III}}_{\mathrm{LS}}$ and ${}^{P/F}\mathrm{Fe}^{\mathrm{III}}_{\mathrm{LS}}$ XMCD signals are given in Supporting Information **(S.I. section VIII)**.

We normalized the obtained $\left[\sigma^{AF}_{XMCD}\right]^{raw}$ and $\left[\sigma^{P/F}_{XMCD}\right]^{raw}$ XMCD signals in order to define two reference XMCD signals for antiferromagnetic (named σ^{AF}_{XMCD}) and paramagnetic/ferromagnetic $\mathrm{Fe}^{\mathrm{III}}_{\mathrm{LS}}$ ions (named $\sigma^{P/F}_{XMCD}$), such that at $\boldsymbol{B} = 6.5$ T, the intensity of peak α is equal to respectively +0.8 (-0.8) for σ^{AF}_{XMCD} ($\sigma^{P/F}_{XMCD}$) where 0.8 is the intensity of peak α for $K_3[Fe(CN)_6]$ at 6.5 T (see Figure 6, lower panel). The procedure to extract both σ^{AF}_{XMCD} and $\sigma^{P/F}_{XMCD}$ signals mainly rests on the idea that when the Fe ions are fully

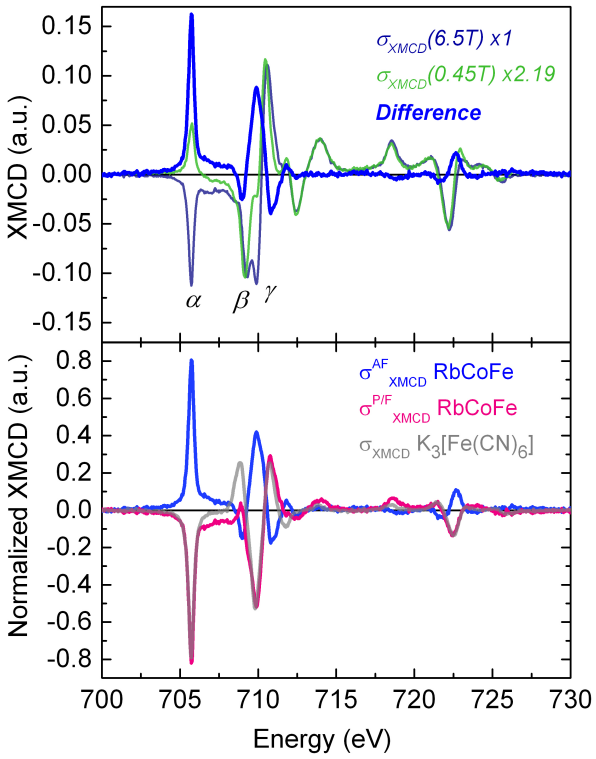

Figure 6: (Top) Difference of the two XMCD signals at Fe $L_{2,3}$ edges (blue line) recorded at $\boldsymbol{B} = 6.5$ T and 0.45 T. The XMCD signal at $\boldsymbol{B} = 0.45$ T is normalized so that peak β superimpose with the one from the XMCD signal at $\boldsymbol{B} = 6.5$ T. (Bottom) Fe^{III}_{LS} reference XMCD signals: σ^{AF}_{XMCD} and $\sigma^{P/F}_{XMCD}$, together with the XMCD signal of $K_3[Fe(CN)_6]$ measured at the Fe $L_{2,3}$ edges at 2 K and 6.5 T.

saturated in either the antiferromagnetic phase or in the paramagnetic/ferromagnetic phase the magnetic moment per Fe ions (in absolute value) should be almost the same as the one measured for fully saturated Fe ions in $K_3[Fe(CN)_6]$. The σ^{AF}_{XMCD} and $\sigma^{P/F}_{XMCD}$ signals have very close shape with some small differences which indicate that the $^{AF}Fe^{III}_{LS}$ and $^{P/F}Fe^{III}_{LS}$ ions have almost the same local environment, close to the one in $K_3[Fe(CN)_6]$. The Fe^{III}_{LS} XMCD signal in the **RbCoFe** photo-excited state at the different magnetic inductions can be reconstructed by linear combination of σ^{AF}_{XMCD} and $\sigma^{P/F}_{XMCD}$:

$$\sigma_{XMCD}(\boldsymbol{B}) = c^{AF}(\boldsymbol{B})\ \sigma^{AF}_{XMCD} + c^{P/F}(\boldsymbol{B})\ \sigma^{P/F}_{XMCD} \tag{1}$$

Varied linear combinations are presented in Supporting Information **(S.I. Figure S10)** and they clearly explain the singular shape of the Fe^{III}_{LS} XMCD signals. Moreover we can reproduce the small intensity of the XMCD signal at 6.5 T, compared to the one expected for a fully saturated XMCD signal for a Fe^{III}_{LS} ion (see section above). The values of $c^{AF}(\boldsymbol{B})$ and $c^{P/F}(\boldsymbol{B})$ in Eq.1 at the measured external inductions are reported in Figure 7 It is important to note that because it has been possible to determine σ^{AF}_{XMCD} (resp. $\sigma^{P/F}_{XMCD}$), the values of the $c^{AF}(\boldsymbol{B})$ coefficients (resp. $c^{P/F}(\boldsymbol{B})$ coefficients) are a direct measurement of the Fe magnetization present in the antiferromagnetic phase (resp. in the paramagnetic/ferromagnetic phase). At 6.5 T, where the absolute magnetization of ${}^{AF}Fe^{III}_{LS}$ and ${}^{P/F}Fe^{III}_{LS}$ should be equal, the coefficients give the fraction of antiferromagnetic and paramagnetic/ferromagnetic ions: the population of ${}^{AF}Fe^{III}_{LS}$ ($c^{AF}(6.5\mathrm{T}) = 0.43$) is slightly lower than the ${}^{P/F}Fe^{III}_{LS}$ one ($c^{P/F}(6.5\mathrm{T}) = 0.56$) **(see S.I Table 1)**. The close amount of ${}^{P/F}Fe^{III}_{LS}$ and ${}^{AF}Fe^{III}_{LS}$ species, which has been hypothesized above, is experimentally confirmed. The $c^{AF}(\boldsymbol{B})$ curve follows the magnetization curve of the ${}^{AF}Fe^{III}_{LS}$ ions, while the $c^{P/F}(\boldsymbol{B})$ curve follows the magnetization curve of the ${}^{P/F}Fe^{III}_{LS}$ ions.

Since the σ^{AF}_{XMCD} and $\sigma^{P/F}_{XMCD}$ signals have opposite signs, the difference curve $c^{P/F}(\boldsymbol{B}) - c^{AF}(\boldsymbol{B})$ follows the total Fe^{III} XMCD-detected magnetization curve and the sum curve $c^{P/F}(\boldsymbol{B}) + c^{AF}(\boldsymbol{B})$ follows the total Co^{II} XMCD-detected magnetization curve. This is indeed what is observed (**S.I. Figure S12**). The $c^{AF}(\boldsymbol{B})$ curve in Figure 7 presents a sharp rise from 0 to 0.45 T and a very moderate rise between 1.5 T to 6.5 T. This shape is in agreement with the hypothesis of antiferromagnetic coupling. The $c^{P/F}(\boldsymbol{B})$ curve presents also a sharp rise from 0 to 0.45 T and continue to increase significantly after 1.5 T. The large slope of $c^{P/F}(\boldsymbol{B})$ at low induction would tend to evidence some ferromagnetic interaction. To verify this hypothesis, we performed LFM calculations for a Fe^{III}_{LS} in O_h symmetry using a two configuration MLCT model to account for π back bonding of the cyanido ligand, as described elsewhere.[40,41] In the Hamiltonian, the effect of the external magnetic induction and the exchange are described by:

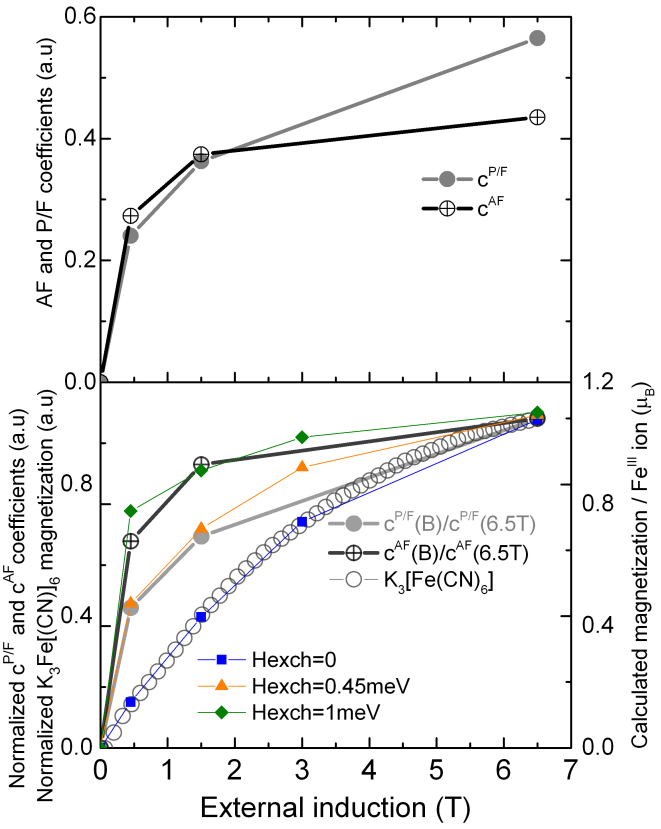

Figure 7: Coefficients $c^{AF}(\boldsymbol{B})$ (black line with $\oplus$) and $c^{P/F}(\boldsymbol{B})$ (grey line with $\bullet$) curves compared with $K_3[Fe(CN)_6]$ XMCD detected magnetization curve ($\circ$) and with theoretical magnetization curves calculated with LFM model for Fe^{III}_{LS} ion with exchange magnetic energies equal to 0 ($\blacksquare$), 0.45 meV ($\blacktriangle$) and 1.0 meV ($\blacklozenge$).

$$H = \mu_B(L_z + g_0 S_z)\boldsymbol{B_{ext}} + \mu_B g_0 S_z \boldsymbol{B_{exch}} \quad (2)$$

where μ_B is the Bohr magneton ($\mu_B = 5.78838.10^{-5} eV/T$), $g_0 \approx 2$ is the electron Landé factor, $\boldsymbol{B_{ext}}$ is the external induction and $\boldsymbol{B_{exch}}$ is the local exchange magnetic field resulting from the magnetic interaction between the Fe^{III} ion and its Co^{II}neighbors. From the calculation of the initial eigenstates ($|i\rangle$) for Fe^{III}_{LS} ion, one gets the expectation values $\langle L_z\rangle = \langle i|L_z|i\rangle$ and $\langle S_z\rangle = \langle i|S_z|i\rangle$. The total magnetic moment in the $|i\rangle$ state is $m_i = -(\langle L_z\rangle + 2\langle S_z\rangle)\mu_B$. The magnetic moment at a given temperature T is calculated with a Boltzmann distribution **(see S.I. section IX)**. The magnetization curves (*i.e.* the variation of the magnetic moment with the external induction) were calculated at T = 2 K with different values of the exchange field (**see S.I. S13**) for one Fe^{III} ion. For comparison, the calculated magnetizations for the AF phase (resp. P/F phase) are multiplied by 0.56 (resp. 0.43) to account for the repartition of Fe ions between the two phases. Comparison between the $c^{AF}(\boldsymbol{B})$ and $c^{P/F}(\boldsymbol{B})$ curves and the LFM calculated magnetization is shown in Figure 7. The shape of the $c^{AF}(\boldsymbol{B})$ curve is well reproduced using an exchange energy of $\mu_B g_0 \boldsymbol{B_{exch}} \simeq 1.0\ meV$ (equivalent to 8.1 cm^{-1}). To reproduce the slope of the $c^{P/F}(\boldsymbol{B})$, it is necessary to include an exchange energy $\mu_B g_0 \boldsymbol{B_{exch}} \simeq 0.45\ meV$ (equivalent to 3.63 cm^{-1}). The comparison with the calculation for a paramagnetic Fe ion with no exchange magnetic field as well as with the experimental curve measured for $K_3[Fe(CN)_6]$ clearly indicates that the exchange field for the P/F phase is necessary. This clearly evidences that the Fe^{III}_{LS} ions with the magnetic moment parallel to the magnetic induction are in ferromagnetic interaction with the Co^{II}_{HS} ions.

Discussion : Probing the Co^{II}_{HS}-Fe^{III}_{LS} magnetic interaction in the photo-excited state

In addition of being an element-selective probe of the electronic structure and the local magnetic moment, XAS and XMCD at the $L_{2,3}$ edges of transition metal ions are mainly sensitive to the sample surface when they are detected in total electron yield (TEY). This was not the case for most of the techniques that have been used so far to study photomagnetic CoFe Prussian blue analogues. The TEY detection mode probes the first ≈5 nm below the surface which corresponds to ≈10 metallic layers along the [001] direction. This is the reason why the present results allow us to revisit the description of the photomagnetic **RbCoFe** Prussian Blue Analogue and especially the description of the sample surface. Given the lack of information on the exact depth of sample that is probed by X-rays and on the interface between the two well-defined core and surface parts of the sample, we will not try to give a quantitative description in terms of number of metallic layers.

The present XMCD study clearly shows that the photo-excited state of **RbCoFe** contains two different and very well defined Fe^{III}_{LS} sites. Both Fe^{III}_{LS} sites differ from each other 1by slightly different structures and very different magnetic behaviors, which allows us to conclude that they correspond to two well-defined parts of the sample. One part of the sample exhibits the behavior that was already evidenced by previous studies realized by techniques probing the whole sample volume. This part of the sample corresponds to the core of the particles and it is mainly composed of $Co^{III}_{LS}Fe^{II}_{LS}$ pairs in its ground state and of $Co^{II}_{HS}Fe^{III}_{LS}$ ones in the photo-excited state. Below the Curie temperature ($T_C \approx 21\ K$), the exchange interaction between the Co^{II}_{HS} and Fe^{III}_{LS} ions is antiferromagnetic. The largest magnetic moments borne by the Co^{II}_{HS} ions are parallel to the external magnetic induction and the magnetization of this part of the sample dominates the Fe magnetization curve below 1.5 T. The exchange energy of 1.0 meV ($\approx$ 12 K.k_B) evaluated from the LFM calculations is in the same order of magnitude as the value roughly determined from magnetic measure-

ments ($T_C \approx 21\ K$). Assuming 1 Fe^{III} ion in interaction with z Co^{II} ($1 \leq z \leq 6$), with a J exchange coupling constant, we can write $g_0\mu_B \boldsymbol{B_{exch}} \approx zJS_{Co^{II}} = 3/2zJ$ and, making the same assumption as Goujon and coworkers[13] ($T_C \approx zJ$), we obtain $g_0\mu_B \boldsymbol{B_{exch}}/k_B \approx 30$ K, which is in reasonable agreement with the value determined from LFM. We propose to assign the other well-defined part of the sample to the surface of the particles. Such a surface part of the sample has only been mentioned so far in some studies of photomagnetic CoFe PBA nanoparticles.[43,44] This surface part of the sample is mainly composed of $Co^{II}_{HS}Fe^{III}_{LS}$ pairs in both the ground state and the metastable excited state. At low temperature, the exchange interaction between the Co^{II}_{HS} and Fe^{III}_{LS} ions is ferromagnetic. As in the antiferromagnetic core, the largest magnetic moments borne by the Co^{II}_{HS} ions are parallel to the external magnetic induction and the magnetization of this part of the sample dominates the Fe magnetization curve above 1.5 T. The exchange energy determined from the LFM calculations is of 0.45 meV (≈ 5 K.k_B).

Thus, at low temperature, the metastable photo-excited state of **RbCoFe** can be described as a ferrimagnetic $Co^{II}_{HS}Fe^{III}_{LS}$ core surrounded by a ferromagnetic $Co^{II}_{HS}Fe^{III}_{LS}$ shell made of some metallic layers. This magnetic core-shell structure of the metastable photo-excited state can be related to the electronic structure of the metal ions and to the geometry of the $Co^{II}_{HS}Fe^{III}_{LS}$ linkages. Verdaguer *et al.*[47] applied the orbital models proposed by Hoffman *et al.*[48] or Kahn *et al.*[49] to foresee Curie temperatures and the nature of the exchange interaction in Prussian Blue Analogues. With one t_{2g} singly occupied orbital for the Fe ion and one t_{2g} and two e_g singly occupied orbitals for the Co ion, one can predict a strong competition between one t_{2g}-t_{2g} pathway, leading to antiferromagnetic interactions, and two t_{2g}-e_g pathways, leading to ferromagnetic interactions. This results in CoFe PBAs either in weak ferrimagnetism or in weak ferromagnetism. As the exchange interaction is directly linked to the overlap between the magnetic orbitals, slight structural differences in the geometry of the Co-NC-Fe linkages would be likely to modify the sign of J. Indeed, the XMCD study clearly shows that the two Fe sites in the antiferromagnetic phase and in the ferromagnetic phase

both resemble much the site for Fe in $K_3[Fe(CN)_6]$. The strange shape and intensity of the XMCD signal measured at the Fe $L_{2,3}$ edges is the consequence of an almost equipartition of the Fe ions between this two phases. The two slightly different structures are most probably associated with slightly different geometries of the Co-NC-Fe linkages in the core and in the shell, which may be the source of the different exchange interactions.

Conclusion

In this work, the photo-excited state of the $Rb_2Co_4[Fe(CN)_6]_{3.3} \cdot 11\,H_2O$ PBA was investigated by element specific $L_{2,3}$ edges XAS and XMCD. The XMCD measurements at the Co and Fe $L_{2,3}$ edges, probing the magnetic $3d$ orbitals, have provided a direct evidence of the antiferromagnetic interaction between the Co^{II}_{HS} and the Fe^{III}_{LS} ions belonging to the core of the 100 nm particles. They confirm the previously published results obtained from XMCD measurements at the Co and Fe K edges, which were only an indirect proof of the antiferromagnetic interaction. Transition metal K-edge XMCD indeed measures only the orbital magnetic moment of the $4p$ electrons and not the spin magnetic moment of the $3d$ electrons. Thanks to the surface sensitivity of the $L_{2,3}$ edges measured in TEY, the magnetic properties at the surface have also been revealed. Surface species exhibit a peculiar magnetic behavior different from that of the core. Indeed, the Co^{II}_{HS} and Fe^{III}_{LS} ions at the surface are in weak ferromagnetic interaction, probably due to a slightly different geometry of the Co–NC–Fe linkages at the surface of the particles. Thus, the magnetic structure of the photomagnetic **RbCoFe** 100 nm particles can be described as a ferrimagnetic core surrounded by a ferromagnetic shell. This raises the question of the nature of the magnetic interaction in photomagnetic nanoparticles of CoFe PBA, where surface is expected to strongly influence the magnetic properties, and also for molecular CoFe PBAs such as the cube,[50] the square,[8,11,51–54] or the dinuclear[55,56] complexes that have been recently synthesized and where the magnetic exchange paths are strongly reduced compared to the three-dimensionnal

PBAs.

Acknowledgement

This work was supported by the Centre National de la Recherche Scientifique (CNRS, France), the Ministère de l'Enseignement Supérieur et de la Recherche (MESR, France), and the GDR MCM-2 French research group. The authors acknowledge SOLEIL for provision of synchrotron radiation facilities through proposal 99130220, the DEIMOS beamline staff for technical and scientific support during experiments, and Loïc Joly (IPCMS) for computing support at DEIMOS. We thank Patricia Beaunier (LRS) for transmission electron microscopy measurements, Eric Rivière (ICMMO) for the preparation of the laser setup installed on DEIMOS, Lorenzo Paulatto, Alain Soyer and Benoit Baptiste (IMPMC) for computing support or for helpful discussion on crystallography.

Supporting Information Available

X-ray diffraction, Transmission Electron Microscopy, SQUID magnetic measurements and XAS at Co and Fe K edges for **RbCoFe**. Detailed analysis of the experimental spectra and detailed calculations within LFM theory. This material is available free of charge via the Internet at `http://pubs.acs.org/`.

References

(1) Sato, O.; Tao, J.; Zhang, Y.-Z. *Angewandte Chemie International Edition* **2007**, *46*, 2152–2187.

(2) Aguilà, D.; Prado, Y.; Koumousi, E. S.; Mathonière, C.; Clérac, R. *Chem. Soc. Rev.* **2016**, *45*, 203–224.

(3) Champion, G.; Escax, V.; Cartier dit Moulin, C.; Bleuzen, A.; Villain, F.; Baudelet, F.; Dartyge, E.; Verdaguer, M. *Journal of the American Chemical Society* **2001**, *123*, 12544–12546.

(4) Sato, O.; Iyoda, T.; Fujishima, A.; Hashimoto, K. *Science* **1996**, *272*, 704–705.

(5) ichi Ohkoshi, S.; Tokoro, H.; Hashimoto, K. *Coordination Chemistry Reviews* **2005**, *249*, 1830 – 1840, 36th International Conference on Coordination Chemistry, Merida, Mexico, July 2004.

(6) Papanikolaou, D.; Margadonna, S.; Kosaka, W.; Ohkoshi, S.-i.; Brunelli, M.; Prassides, K. *Journal of the American Chemical Society* **2006**, *128*, 8358–8363, PMID: 16787101.

(7) Avendano, C.; Hilfiger, M. G.; Prosvirin, A.; Sanders, C.; Stepien, D.; Dunbar, K. R. *Journal of the American Chemical Society* **2010**, *132*, 13123–13125, PMID: 20809572.

(8) Zhang, Y.; Li, D.; Clérac, R.; Kalisz, M.; Mathonière, C.; Holmes, S. M. *Angewandte Chemie International Edition* **2010**, *149*, 3752–3756.

(9) Funck, K. E.; Prosvirin, A. V.; Mathoniere, C.; Clerac, R.; Dunbar, K. R. *INORGANIC CHEMISTRY* **2011**, *50*, 2782–2789.

(10) Liu, T.; Dong, D.-P.; Kanegawa, S.; Kang, S.; Sato, O.; Shiota, Y.; Yoshizawa, K.; Hayami, S.; Wu, S.; He, C.; Duan, C.-Y. *Angewandte Chemie International Edition* **2012**, *51*, 4367–4370.

(11) Mondal, A.; Li, Y.; Seulaiman, M.; Julve, M.; Toupet, L.; Marylise, B.-L. C.; Lescouëzec, R. *Journal of the American Chemical Society* **2013**, *135*, 1653–1656.

(12) Sato, O.; Einaga, Y.; Fujishima, A.; Hashimoto, K. *Inorganic Chemstry* **1999**, *38*, 4405–4412.

(13) Goujon, A.; Roubeau, O.; Varret, F.; Dolbecq, A.; Bleuzen, A.; Verdaguer, M. *The European Physical Journal B* **2000**, *14*, 115–124.

(14) Shimamoto, N.; Ohkoshi, S.-i.; Sato, O.; Hashimoto, K. *Inorganic Chemistry* **2002**, *41*, 678–684.

(15) Escax, V.; Cartier dit Moulin, C.; Villain, F.; Champion, G.; Itié, J.-P.; Münsch, P.; Verdaguer, M.; Bleuzen, A. *Comptes Rendus Chimie* **2003**, *6*, 1165–1173.

(16) Bleuzen, A.; Lomenech, C.; Escax, V.; Villain, F.; Varret, F.; Cartier dit Moulin, C.; Verdaguer, M. *Journal of the American Chemical Society* **2000**, *122*, 6648–6652.

(17) Escax, V.; Bleuzen, A.; Cartier dit Moulin, C.; Villain, F.; Goujon, A.; Varret, F.; Verdaguer, M. *Journal of the American Chemical Society* **2001**, *123*, 12536–12543.

(18) Bleuzen, A.; Escax, V.; Ferrier, A.; Villain, F.; Verdaguer, M.; Münsch, P.; Itié, J.-P. *Angewandte Chemie International Edition* **2004**, *43*, 3728–3731.

(19) Bleuzen, A.; Cafun, J.-D.; Bachschmidt, A.; Verdaguer, M.; Münsch, P.; Baudelet, F.; Itié, J.-P. *Journal of Physical Chemistry C* **2008**, *112*, 17709–17715.

(20) Bleuzen, A.; Escax, V.; Itié, J.-P.; Münsch, P.; Verdaguer, M. *Comptes Rendus Chimie* **2003**, *6*, 343–352.

(21) Bleuzen, A.; Marvaud, V.; Mathonière, C.; Sieklucka, B.; Verdaguer, M. *Inorganic Chemistry* **2009**, *48*, 3453–3466.

(22) Le Bris, R.; Cafun, J.-D.; Mathonière, C.; Bleuzen, A.; Létard, J.-F. *New Journal of Chemistry* **2009**, *33*, 1255–1261.

(23) Cafun, J.-D.; Cartier dit Moulin, C.; Fornasieri, G.; Arrio, M.-A.; Briois, V.; Bleuzen, A. *New Journal of Chemistry* **2011**, *35*, 2074–2080.

(24) Cafun, J.-D.; Lejeune, J.; Baudelet, F.; Dumas, P.; Itié, J.-P.; Bleuzen, A. *Angewandte Chemie International Edition* **2012**, *51*, 9146–9148.

(25) Lejeune, J.; Cafun, J.-D.; Fornasieri, G.; Brubach, J.-B.; Creff, G.; Roy, P.; Bleuzen, A. *European Journal of Inorganic Chemistry* **2012**, *2012*, 3980–3983.

(26) Cafun, J.-D.; Champion, G.; Arrio, M.-A.; Cartier dit Moulin, C.; Bleuzen, A. *Journal of the American Chemical Society* **2010**, *132*, 11552–11559.

(27) Cartier dit Moulin, C.; Villain, F.; Bleuzen, A.; Arrio, M.-A.; Sainctavit, P.; Lomenech, C.; Escax, V.; Baudelet, F.; Dartyge, E.; Gallet, J.-J.; Verdaguer, M. *Journal of the American Chemical Society* **2000**, *122*, 6653–6658.

(28) Cartier dit Moulin, C.; Champion, G.; Cafun, J.-D.; Arrio, M.-A.; Bleuzen, A. *Angewandte Chemie International Edition* **2007**, *46*, 1–4.

(29) Escax, V.; Bleuzen, A.; Itié, J.-P.; Münsch, P.; Varret, F.; Verdaguer, M. *Journal of Physical Chemistry B* **2003**, *107*, 4763–4767.

(30) Varret, F.; Constant-Machado, H.; Dormann, J.; Goujon, A.; Jeftic, J.; Noguès, M.; Bousseksou, A.; Klokishner, S.; Dolbecq, A.; Verdaguer, M. *Hyperfine interactions* **1998**, *113*, 37–46.

(31) Pajerowski, D. M.; Garlea, V. O.; Knowles, E. S.; Andrus, M. J.; Dumont, M. F.; Calm, Y. M.; Nagler, S. E.; Tong, X.; Talham, D. R.; Meisel, M. W. *Physical Review B* **2012**, *86*.

(32) Funk, T.; Deb, A.; George, S. J.; Wang, H.; Cramer, S. P. *Coordination Chemistry Reviews* **2005**, *249*, 3–30.

(33) van der Laan, G.; Figueroa, A. I. *Coordination Chemistry Review* **2014**, *277*, 95–129.

(34) Moulin, R.; Delahaye, E.; Bordage, A.; Fonda, E.; Baltaze, J.-P.; Beaunier, P.; Riviere, E.; Fornasieri, G.; Bleuzen, A. *European Journal of Inorganic Chemistry* **2017**, 1303–1313.

(35) Ohresser, P. et al. *Review of Scientific Instruments* **2014**, *85*.

(36) Chen, C. T.; Idzerda, Y. U.; Lin, H.-J.; Smith, N. V.; Meigs, G.; Chaban, E.; Ho, G. H.; Pellegrin, E.; Sette, F. *Phys. Rev. Lett.* **1995**, *75*, 152–155.

(37) de Groot, F. M. F.; Fuggle, J. C.; Thole, B. T.; Sawatzky, G. A. *Phys. Rev. B* **1990**, *42*, 5459–5468.

(38) Cowan, R. D. *The theory of atomic structure and spectra*; Univ. of California Press: Berkeley, CA, 1981; Vol. 3.

(39) Butler, P. H. *Point group symmetry applications: methods and tables*; Springer Science & Business Media: New York, 2012.

(40) Hocking, R. K.; Wasinger, E. C.; de Groot, F. M. F.; Hodgson, K. O.; Hedman, B.; Solomon, E. I. *J. Am. Chem. Soc.* **2006**, *128*, 10442–10451.

(41) Jafri, S. F.; ; Koumousi, E. S.; Sainctavit, P.; Juhin, A.; Schuler, V.; Bunao, O.; Dmitri, M.; Dechambenoite, P.; Mathonière, C.; Clérac, R.; Otero, E.; Ohresser, P.; Cartier dit Moulin, C.; Arrio, M.-A. *Inorganic Chemistry* **2016**, *55*, 6980–6987.

(42) Escax, V.; Champion, G.; Arrio, M.-A.; Zacchigna, M.; Cartier dit Moulin, C.; Bleuzen, A. *Angewandte Chemie International Edition* **2005**, *44*, 4798–4801.

(43) Aouadi, M.; Fornasieri, G.; Briois, V.; Durand, P.; Bleuzen, A. *Chemistry - A European Journal* **2012**, *18*, 2617–2623.

(44) Pajerowski, D. M.; Frye, F. A.; Talham, D. R.; Meisel, M. W. *New Journal of Physics* **2007**, *9*.

(45) Arrio, M. A.; Sainctavit, P.; Cartier dit Moulin, C.; Mallah, T.; Verdaguer, M.; Pellegrin, E.; Chen, C. T. *J. Am. Chem. Soc.* **1996**, *118*, 6422–6427.

(46) Prado, Y.; Arrio, M.-A.; Volatron, F.; Otero, E.; CartierditMoulin, C.; Sainctavit, P.; Catala, L.; Mallah, T. *Chemistry – A European Journal* **2013**, *19*, 6685–6694.

(47) Verdaguer, M.; Bleuzen, A.; Marvaud, V.; Vaissermann, J.; Seuleiman, M.; Desplanches, C.; Scuiller, A.; Train, C.; Garde, R.; Gelly, G.; Lomenech, C.; Rosenman, I.; Veillet, P.; Cartier, C.; Villain, F. *Coordination Chemistry Reviews* **1999**, *190*, 1023 – 1047.

(48) Hay, P. J.; Thibeault, J. C.; Hoffmann, R. *Journal of the American Chemical Society* **1975**, *97*, 4884–4899.

(49) Girerd, J. J.; Journaux, Y.; Kahn, O. *Chemical Physics Letters* **1981**, *82*, 534 – 538.

(50) Li, D.; Clérac, R.; Roubeau, O.; Harte, E.; Mathonière, C.; Le Bris, R.; Holmes, S. M. *Journal of the American Chemical Society* **2008**, *130*, 252–258.

(51) Mercurol, J.; Li, Y.; Pardo, E.; Risset, O.; Seuleiman, M.; Rousseliere, H.; Lescouëzec, R.; Julve, M. *Chemical Communications* **2010**, *46*, 8995–8997.

(52) Zhang, Y.; Ferko, P.; Siretanu, D.; Ababei, R.; Rath, N. P.; Shaw, M. J.; Clérac, R.; ; Mathonière, C.; Holmes, S. M. *Journal of the American Chemical Society* **2014**, *136*, 168954–16864.

(53) Nihei, M.; Sekine, Y.; Suganami, N.; Oshio, H. *Chemistry Letters* **2010**, *39*, 978–979.

(54) Nihei, M.; Sekine, Y.; Suganami, N.; Nakazawa, K.; Nakao, A.; Murakami, Y.; Oshio, H. *Journal of the American Chemical Society* **2011**, *133*, 3592–3600.

(55) Jeon, I.-R.; Calancea, S.; Panja, A.; Cruz, D. M. P.; Koumousi, E. S.; Dechambenoit, P.; Coulon, C.; Wattiaux, A.; Rosa, P.; Mathonière, C.; Clérac, R. *Chemical Science* **2013**, *4*, 2463–2470.

(56) Koumousi, E. S.; Jeon, I.-R.; Gao, Q.; Dechambenoit, P.; Woodruff, D. N.; Merzeau, P.; Lionel, B.; Jia, X.; Li, D.; Volatron, F.; Mathonière, C.; Clérac, R. *Journal of the American Chemical Society* **2010**, *136*, 15461–15464.

Graphical TOC Entry